Institute of Geodesy and Geoinformation

Theoretical Geodesy Group

Towards the Development of a Continuous Spatio-Temporal Finite Element Based Representation of the Mean Sea Surface

Technical Reports of the Theoretical Geodesy Group

IGG-TG-2022-01

Moritz Borlinghaus (corresponding author)
Institute of Geodesy and Geoinformation, University of Bonn
Nussallee 17, D-53115 Bonn, Germany
borlinghaus@geod.uni-bonn.de

Christian Neyers
Institute of Geodesy and Geoinformation, University of Bonn
Nussallee 17, D-53115 Bonn, Germany
neyers@geod.uni-bonn.de

Jan Martin Brockmann
Institute of Geodesy and Geoinformation, University of Bonn
Nussallee 17, D-53115 Bonn, Germany
brockmann@geod.uni-bonn.de

Bonn 2022

igg

UNIVERSITÄT BONN

Abstract

The mean sea surface has an important role both in the calculation of the mean dynamic topography and in the area of sea level change as a reference surface. This paper presents a new approach to estimate a continuous spatio-temporal mean sea surface from along-track altimetric sea surface height measurements. A parametric function continuously defined in the spatial as well as temporal domain is constructed from a C^1-smooth finite element space to represent the mean sea surface. Least-squares observation equations are set up, to estimate the unknown scaling coefficients from the sea surface height measurements as collected by altimetric exact repeat missions and geodetic missions. An advantage of the proposed method is that the surface is represented by an analytic model and the unknown parameters can be physically interpreted. Whereas the static component of the function represents the mean sea surface, the temporal component is used to absorb the ocean variability.

Within a proof-of-concept study 10 years of satellite altimetry from CryoSat–2 and Jason 1–3 over the period 2010 to 2019 are used and analyzed in two study regions with different spatial resolutions. Besides the static mean sea surface, the temporal component which is estimated covers a linear trend and the annual period. The comparison of the static component to the global CNES_CLS15 MSS shows a reasonable agreement with a root mean square error below 10 cm over the entire North Atlantic. But still, systematic differences occur especially in regions with a high temporal variability. Comparisons of the temporal component with gridded sea level anomaly products show a good agreement in areas of low ocean variability, but highlights that in regions of large ocean variability the temporal basis function chosen in this initial study must be further investigated. In general, it is demonstrated that the proposed approach can be an alternative to the well established mean sea surface estimation procedures.

Keywords Mean sea surface · Finite elements · Satellite altimetry · Sea level variations · Ocean variability · C^1-smoothness

Chapter 1

Introduction

The Mean Sea Surface (MSS) as the spatial and temporal average of the actual sea surface is used as a reference surface in oceanography, but also in geodesy. In this context, it finds applications, for example, in the computation of bathymetric maps (see e.g. Dixon et al., 1983; Smith and Sandwell, 1994), in the geodetic computation of the mean dynamic ocean topography, which can be used to detect and analyze global long-term stable ocean currents (e.g. Knudsen et al., 2011; Becker et al., 2014; Mulet et al., 2021), or in general sea level studies (e.g. Chen et al., 2000; Uebbing et al., 2019).

A common method of calculating the MSS in geodesy is a grid based spatial and temporal averaging of along-track Sea Surface Height (SSH) observations measured by satellites with altimeters in a given period. A major challenge in calculating the MSS is the temporal variability of the sea surface (e.g. Andersen and Knudsen, 2009; Schaeffer et al., 2012; Agha Karimi et al., 2020), which – due to temporal aliasing – can cause local biases in the MSS models.

At this point, it becomes important to distinguish between the observations of the exact repeat missions (ERM) and the geodetic missions (or geodetic mission phases, GM). Whereas the ERM like Topex/Poseidon or the Jason family have a short repeat phase of just 10 days, the GM have a long repeat, which is typically above one year. Consequently, ERM missions have a poor spatial coverage, as the track spacing is large. Contrary, GM missions are important for the spatial coverage, but suffer from a poor temporal resolution (e.g. Andersen et al., 2021).

For the ERM, the elimination of the temporal ocean variability from the SSH observations for MSS modeling is straightforward. Temporal averaging of complete cycles, linked to a reference track, directly removes the periodic short term signals and yields the mean profile of the MSS along the reference track. The spatial processing can be performed in an independent second step, e.g. the prediction to a smoothed regular spatial grid. Unfortunately, this approach can not be applied to the GM observations, as the – especially seasonal – variations do not cancel due to the repeat cycle larger than a year. Consequently, spatial and temporal averaging must be performed either i) in a joint analysis of ERM and GM data or ii) the temporal characteristics must be determined from complementary information (e.g. ERM-only or model data) and reduced within a preprocessing step ahead of the spatial analysis (e.g. Schaeffer et al., 2012; Agha Karimi et al., 2020) from the SSH measurements observed by the GM.

Several methods have been developed to deal with the temporal variability of SSH, which is mainly attributed to oceanic variability. In Agha Karimi et al. (2020) a spectral analysis is used to correct CryoSat–2 altimetric observations to estimate a regional MSS around Australia. The analysis is applied to the ERM sea level anomalies (SLA - difference between SSH and a model of the MSS) which is performed independently in manually chosen sub-regions. From these data, annual and semi-annual amplitudes and phases are estimated, which are spatially interpolated to the CryoSat–2 tracks. Afterwards the CryoSat–2 SLA are corrected with the annual and semi-annual signals derived from the ERM. The final MSS is obtained by spatially averaging the corrected SLA in gridded $0.1°\times0.1°$ cells and restoring the MSS model reduced previously.

Many other approaches use a-priori daily or monthly SLA grids (cf. Traon et al., 1998; Ducet et al., 2000) as distributed for instance by AVISO to correct the altimetric observations for the

high frequency variability. Different approaches which use these maps are briefly presented below.

To compute the DNSC08 (Andersen and Knudsen, 2009) 12 years of multi-mission satellite altimetry observations are used. The method is based on a two-step procedure, the first step is to estimate a long-wavelength MSS from the temporally averaged mean profiles of the ERM missions. In order to estimate the short wavelengths of the MSS, mainly the GM observations are used. The initial long-wavelength MSS serves as a reference model in a remove-compute-restore approach applied in the second step. For this purpose, every track is adjusted to the long-wavelength MSS using a crossover analysis for overlapping $4° \times 12°$ boxes. After that, the MSS is interpolated on a $1/60°$ grid and then assembled to the final MSS. For the computation of the successor MSS (DTU13 and DTU18, cf. Andersen et al., 2015, 2018) a similar method was applied. But, in Andersen et al. (2018) interpolated daily SLA maps are used to correct the GM observations for inter-annual and seasonal oceanic variability.

Schaeffer et al. (2012) and Pujol et al. (2018) apply a slightly different approach to reduce the oceanic variability for determination of CNES_CLS11 and CNES_CLS15 MSS models. Schaeffer et al. (2012) uses a collocation technique, the so called Optimal Analysis (OA), which allows correcting a given SSH for ocean variability derived from other ERM altimeters that are used as reference. For this, mean profiles are computed for each reference mission, which are merged after that. In the next step, SLA are computed and predicted to a regular gird using covariance functions for the sea surface and the measurement errors (Le Traon and Dibarboure, 2004). Furthermore, OA is used to assign an arbitrary reference epoch to the model. The OA is applied to all SSH of all missions used, even for the ERM before the calculation of the mean profiles. Afterwards, the MSS is computed on a regular grid using a least-squares collocation approach. The determination of CNES_CLS15 MSS follows a similar approach. Instead of OA, ocean variability is reduced by the delayed-time DUACS Level 4 gridded SLA DT2010 maps (Traon et al., 1998; Ducet et al., 2000). For the final model determination, again a least-squares collocation approach is applied and yields the CNES_CLS15 MSS based on 20-years of satellite altimetry.

Besides daily gridded SLA maps there are also monthly averaged gridded sea level variation time series (Traon et al., 1998; Ducet et al., 2000) provided by AVISO. The global MSS model WHU2013 (Jin et al., 2016) uses two different approaches to correct the ocean variability of the non-ERM observations. The first method is based on the monthly gridded SLA time series between 1993 and 2012. Thus, they are used to fit a bias, linear trend, seasonal and annual signals for every point of the grid. Spatial interpolation of the fitted parameters to the location of the non-ERM observations yields a correction model for the observed SSH. For the second approach, mean along-track ERM SSH by a collinear method are used to compute along-track sea surface variation time series. Thus, this time series can be used to correct the sea surface observations of the GM. For this method the location and observation time of available ERM data must be close to that of the non-ERM observations. This method is applied inside $\pm 66°$ region, where the ERM observations are available. Outside this region the first approach is used. For ERM observations, full-year observations are selected to eliminate the seasonal and annual sea level variations in a collinear adjustment. After a crossover adjustment, a least-squares collocation is used to compute the gridded MSS model.

The goal of this manuscript is to present a proof-of-concept study to estimate a continuous spatio-temporal model of the mean sea surface from altimetric SSH observations using time-variable C^1-smooth finite elements as basis functions. Instead of eliminating the temporal variability in a preprocessing step, the temporal signal is parameterized and co-estimated, jointly analyzing the ERM and GM SSH observations within a single adjustment. Whereas the static parameters describe the MSS at a specific reference epoch, the time-dependent parameters model the temporal variability by a predefined set of temporal basis functions. A positive side effect of the chosen parametric representation is that the estimated parameters are physically interpretable. As the analysis can be represented in a one-step least squares estimation, a stochastic model of the SSH measurements can be rigorously propagated to the MSS parameters in a straightforward manner.

The manuscript is organized as follows, in Sect. 2, the theoretical background to construct the C^1-smooth finite element space is provided. Based on the finite element space, the least squares observation equations of a static approximation procedure are constructed. These are extended by

a deterministic model which captures the temporal variations and introduces the new parameters of the spatio-temporal model. Section 3 introduces the two study regions and the data sets analyzed in a proof-of-concept scenario. MSS estimates are derived and discussed for both study areas. Selected analyses are presented to highlight the chances and limits of the proposed procedure and the setup chosen in this initial study. This paper ends with a summary and provides some conclusions in Sect. 4. Additionally, some aspects for future studies are presented.

Chapter 2

Theoretical Background

As discussed in Section 1, the goal in this study is to represent the mean sea surface as a continuous mathematical function. There is no accessible closed expression that is directly derived from physical laws. Instead some function space defined over the domain of interest must be constructed, from which a concrete function can then be estimated in a least-squares adjustment.

To include temporal variability of the sea surface in the model, two independent function spaces, one defined over the spatial domain and the other over the time domain, are combined via the tensor product of their respective bases.

2.1 Finite Element Spaces for Spatial Approximation Tasks

In consideration of the requirements that come with the ocean surface estimation, namely coastal boundaries and relatively high spatial variability, a sensible choice are finite elements on a triangulation in $\mathbb{R}^2$. For constructing these so called Finite Element Spaces (FES), the entire domain of interest is partitioned into a finite number of (in this case triangular) sub-regions, each of which has its own locally defined basis functions and corresponding degrees of freedom (also called parameters). The very definition of a Finite Element is then the shape, the *local* degrees of freedom and the *local* function space spanned by the basis functions of such a sub-region (following Ciarlet, 1978). By means of an appropriate choice of local basis functions, these are usually taken from literature, a piece-wise function space with at least C^0-continuity is achieved. Higher orders of continuity are possible and depend on the actually used Finite Element.

Given a FES definition, a function can then simply be written as

$$g = \sum_{i \in I} a_i b_i \quad g : \mathbb{R}^2 \to \mathbb{R} \tag{2.1.1}$$

where $i \in I$ describes the indexing of all piece-wise defined *global* basis functions $b_i : \mathbb{R}^2 \to \mathbb{R}$, and $a_i \in \mathbb{R}$ the corresponding *global* degrees of freedom/scaling coefficients. The set $\{b_i\}$ of all basis functions is the basis of the FES.

A relational measure for the spatial resolution within a region of fixed size is the number of degrees of freedom, equivalent to the dimension, of the Finite Element (Sub-)Space over that region. Adopting the spatial variability of the expected signal is in general done on a global scale (meaning over the entire domain) by selection of some specific Finite Element and then refined on a local scale by adjusting the size of sub-regions.

2.1.1 Select Finite Elements Applied in this Study

In this study we consider two different sets of local basis functions on triangles, or Finite Elements, both yielding C^1-continuous FES. They differ in both their local degrees of freedom and local function space. The choice of higher continuity comes from the reasonable assumption that the ocean surface is smooth on the scales observable with satellite techniques, in this study specifically altimetry.

The Argyris Element (cf. Argyris et al., 1968) spans a local space of polynomials of degree 5 with 21 degrees of freedom – the function value, the two first and the three second derivatives for each of the three nodes, as well as the three normal derivatives on the centers of the edges. Thus, in addition to the general C^1-continuity, this element guarantees continuity of the second derivatives in the nodes of the triangulation.

In comparison, the Hsieh-Clough-Tocher (HCT) Element (Clough and Tocher, 1966) provides the same continuity with only 12 degrees of freedom. It is from the class of Macro-Elements, where the previously described technique to construct a full FES is similarly applied (one might call it recursively) to an individual element. Based on a further sub-partitioning of a triangle into three sub-triangles, each of which is domain to a polynomial of degree 3, a C^1-continuous piece-wise *local* function space is defined by implicit constraints in the 12 basis functions. These correspond to the 12 degrees of freedom as defined for the whole element, namely the function value and the two first derivatives in each node, as well as the normal derivative at the center point of each edge.

2.1.2 Triangulation

The second major defining factor of a FES is the partitioning of the domain of interest into a mesh, in this study specifically by means of triangulation. It has an immediate effect on the achieved spatial filtering via the size of individual triangles. The coarser the mesh in a particular region the more the signal is filtered and vice versa.

A sophisticated method to generate meshes is developed and implemented in the software library JIGSAW (Engwirda, 2014, 2017, 2019) and can for example be used through its bindings to scripting languages (MATLAB/OCTAVE/PYTHON). It is developed by the Massachusetts Institute of Technology and the NASA to generate very high-quality staggered Voronoi–Delaunay meshes appropriate for various applications in the field of simulations and modeling. The software uses a Frontal-Delaunay refinement technique which allows for the generation of high-quality unstructured spheroidal Delaunay triangulations and uses a hill-climbing-type optimization technique for further grid quality improvement.

It brings the desirable properties of being automatic in its generation of meshes (given some configuration input) and enabling easy local adjustments of triangle density/size as well as geometric constraints.

The important features used for this study are the bounding of the domain of interest with polygons (inner and outer), as well as the so called (discrete) mesh-spacing function. This user-defined function specifies at discrete points (internally completed by interpolation) a target edge length for the triangles which JIGSAW tries to realize by iterative refinement.

In this proof-of-concept study, planar meshes in plate carrée projection with constant mesh-spacing for the whole domain are used. The study regions are restricted by polygons derived from coastline data and straight boundaries over the ocean.

Due to working in the plate carrée projection, triangles are distorted towards the poles and not strictly of equal size with respect to area on the sphere. This can be corrected by employing the ability of JIGSAW to work on a triaxial ellipsoid. Furthermore, regional refinement based on prior information is straightforward, giving possibility to adapt the mesh and consequently the spatial resolution of the FES to regionally varying signal and observation density. These two features are subject to future studies.

2.2 A One-Dimensional Model for the Time Domain

For modeling the temporal behavior of the sea surface, we make the assumption that changes in time are continuous and separable from spatial variability. The latter meaning that at any fixed point in space, the temporal sea surface height change – the SLA – can be represented by a function with the only variable being time (similar to Jin et al., 2016; Agha Karimi et al., 2020). As such

we consider a separate function over time domain

$$h = \sum_{j \in J} c_j d_j \quad h : \mathbb{R} \to \mathbb{R} \tag{2.2.1}$$

where $d_j : \mathbb{R} \to \mathbb{R}$ are the basis functions and $c_j \in \mathbb{R}$ once again the corresponding degrees of freedom/coefficients. We consequently say that $\{d_j\}$ is the set of all temporal basis functions.

It is then necessary to identify basis functions that can model the dominant expected and resolvable temporal variations. Thus our approach in this study is based on a model that is composed of a constant term, a linear term and harmonic terms for the annual signal (again similar to Jin et al., 2016; Agha Karimi et al., 2020). Furthermore, as the assumption of a strictly linear trend is only sensible for sufficiently short periods of time, a simple transformation is introduced that maps a point in time t w.r.t. some reference epoch t_0, i.e. $\Delta t = t - t_0$. This is analogous to a linearization at t_0. The set of temporal basis functions is finally

$$\{d_j\} := \{1, \Delta t, \cos(\omega \Delta t), \sin(\omega \Delta t)\} \tag{2.2.2}$$

where $\omega = \frac{2\pi}{T}$ is the angular frequency of period $T = 365.25\,\mathrm{d}$.

This can easily be extended by additional harmonics to account for other frequencies, e.g. the semi-annual signal, but was omitted for this initial study due to computational constraints. Other feasible choices for the strictly temporal model as discussed in this section include e.g. FES over $\mathbb{R}$ (i.e. usually piece-wise polynomials) or spline function spaces over $\mathbb{R}$.

2.3 A Separately Continuous Spatio-Temporal Model

The final model space is then composed by the tensor product of the spatial with the temporal model space. Given the two sets of basis functions $\{b_i\}$ and $\{d_j\}$, with the tensor product for real-valued functions defined as

$$(g \otimes h)(x, y) = g(x)h(y) \quad x \in \mathbb{R}^n,\ y \in \mathbb{R}^m, \tag{2.3.1}$$

the combined set of basis functions is

$$\{b_i \otimes d_j\} = \{b_i d_j\}\,, \tag{2.3.2}$$

or given in terms of the concrete basis functions $\{d_j\}$

$$\{b_i, b_i \Delta t, b_i \cos(\omega \Delta t), b_i \sin(\omega \Delta t) \mid i \in I\}\,. \tag{2.3.3}$$

Writing a function f in this new basis gives

$$f = \sum_{i \in I} \sum_{j \in J} e_{ij} b_i d_j \quad f : \mathbb{R}^3 \to \mathbb{R};\ (x, y, t) \mapsto f(x, y, t) \tag{2.3.4}$$

with the degrees of freedom/coefficients e_{ij}. In a more explicit form with function arguments and using (2.3.3) this becomes

$$\begin{aligned} f(x, y, t) = &\sum_{i \in I} e_{i0} b_i(x, y) \\ &+ \sum_{i \in I} e_{i1} \Delta t b_i(x, y) \\ &+ \sum_{i \in I} e_{i2} \cos(\omega \Delta t) b_i(x, y) \\ &+ \sum_{i \in I} e_{i3} \sin(\omega \Delta t) b_i(x, y). \end{aligned} \tag{2.3.5}$$

Looking at f with fixed arguments, either for time

$$f_t : (x, y) \mapsto f(x, y, t) \tag{2.3.6}$$

or similarly for space

$$f_{x,y} : t \mapsto f(x, y, t), \tag{2.3.7}$$

it is easy to reason that f is separately continuous, i.e. continuous in time for every point in space and vice versa.

We define

$$f_{\text{mss}} := \sum_{i \in I} e_{i0} b_i = \int_{-\infty}^{\infty} f(x, y, t)\, dt, \tag{2.3.8}$$

describing the static part of the sea surface w.r.t. reference epoch t_0. The equality is straightforward to show. Furthermore we define the time-variable anomalies w.r.t. the static part

$$f_{\text{sla}} := f - f_{\text{mss}}, \tag{2.3.9}$$

containing both the linear trend as well as the annual signal, which represents the temporal model component.

A particular observation in (2.3.4) is the possibility to formulate either time-varying coefficients for $\{b_i\}$ or spatially varying coefficients for $\{d_j\}$, i.e.

$$f = \sum_{i \in I} e_i(t) b_i \qquad e_i(t) := \sum_{j \in J} e_{ij} d_j(t) \tag{2.3.10}$$

or

$$f = \sum_{j \in J} e_j(x, y) d_j \qquad e_j(x, y) := \sum_{i \in I} e_{ij} b_i(x, y). \tag{2.3.11}$$

In this way we can especially depict the spatial variations of the linear trend as well as both amplitude and phase of the (annual) harmonics (cf. Section 3.3.1).

2.4 Estimation Approach

To estimate a concrete model from stochastic observations $\boldsymbol{\mathcal{L}}$ of the sea surface height, here in terms of instantaneous satellite-based altimetry, the standard least-squares adjustment method is applied.

In this initial study, the SSH observations are assumed to be i.i.d. with a variance of σ_0^2, i.e the covariance matrix is

$$\boldsymbol{\Sigma}\{\boldsymbol{\mathcal{L}}\} = \sigma_0^2 \boldsymbol{I}. \tag{2.4.1}$$

The realized measurements l_i are further assumed to be point-wise at location $(x_i, y_i, t_i) := (\lambda_i, \varphi_i, t_i)$ with longitude λ_i, geodetic latitude φ_i and time t_i, for all $i \in \{1 \dots N\}$ with N the number of observations.

As will be further discussed in the following section, data from multiple different satellite missions is used to estimate the models. To account for intermission biases, the observation equations include additional constant bias parameters o_j for the different missions, where one mission is taken as reference with a fixed bias of 0 m.

Thus the observation equations derive with equation (2.3.4) as

$$l_i + v_i = f(\lambda_i, \varphi_i, t_i) + o_j. \tag{2.4.2}$$

For comparison reasons we also estimate strictly spatial models in the form of (2.1.1), yielding the observation equations

$$l_i + v_i = g(\lambda_i, \varphi_i) + o_j. \tag{2.4.3}$$

The vector of unknowns $\boldsymbol{x}$ is then composed of the coefficients $\{e_{ij}, o_j\}$ or $\{a_i,\ o_j\}$, respectively for the spatio-temporal or spatial models.

Chapter 3

Application to Real Data

3.1 Data and Study Area

To obtain a well suited model of the MSS it is important to have data with both a high temporal as well as a high spatial resolution. Whereas the high temporal resolution is required to eliminate the ocean variability by temporal averaging, high spatial resolution is required to model the fine scale MSS signals. To derive a homogeneous model, a comparable spatial distribution over the entire study area is required to make all parameters (cf. Eq. (2.3.5)) estimable.

The time period considered in this study begins in the year 2010 and stops end of 2019. In this period observations of several altimeter missions are available. To obtain the high temporal and spatial resolution, but to keep the number of observations manageable, altimetric SSH measurements from four different satellite missions in the period are selected. The high temporal resolution (from ERM data) is realized using the measurements of the regular mission phases of Jason–2 and Jason–3, as well as the Jason–1 and Jason–2 interleaved mission data (see e.g. ESA, 2020b,c,d). Besides the Jason–1 and Jason–2 GM phases which fall into the period of interest, Low Resolution Mode CryoSat–2 observations are used for their high spatial resolution (see e.g. ESA, 2020a; Andersen et al., 2021). Due to CryoSat–2 having full temporal coverage of the studied time span and its high spatial resolution, it is used as the reference mission for bias estimation. Observations from the L2P data product as processed on behalf of CNES (Centre National d'Etudes Spatiales) SALP project and distributed by AVISO+[1] were used. The applied instrumental and geophysical corrections such as for orbit or tidal errors can be found in the AVISO L2P SLA product handbook (see AVISO, 2017).

Some of the mission characteristics are shown in Table 3.1 (cf. Andersen et al., 2021; ESA, 2020b,c,d,a). Whereas all missions have similar along-track resolution of about 7 km as 1 Hz SSH data are used, the ground track spacing significantly differs. The selected GM have an approximate ground track spacing of 8 km, whereas the ERM's is nearly 315 km at the equator. Because of the low ground track spacing, the GM repeat cycle is relatively large with more than one year. So the ocean variability can not be eliminated by averaging these tracks. For high temporal resolution the ERM and interleaved missions with a repeat cycle of 10 days are needed. These observations allow to eliminate the ocean variability by averaging (e.g. Dibarboure et al., 2012; Becker et al., 2012; Pujol et al., 2018).

Because of the huge amount of along-track observations in the selected time period, two study areas are selected to test and study the performance of the proposed method. Both areas (see Figure 3.1), the North Atlantic up to 80°N (region A) and the Atlantic Ocean and Indian Ocean south of Africa with the Agulhas Current (region B), are selected because of their individual characteristics.

The North Atlantic is characterized by the Gulf Stream (large variability), its island groups (data gaps) and the Arctic region with temporary ice coverage (irregular coverage). But there are also areas dominated by topographic structures with high spatial frequencies. Furthermore, above

[1] For a detailed product description and the procedure to access the data see `https://www.aviso.altimetry.fr/en/data/products/sea-surface-height-products/global/along-track-sea-level-anomalies-l2p.html` (last accessed 01/07/2021).

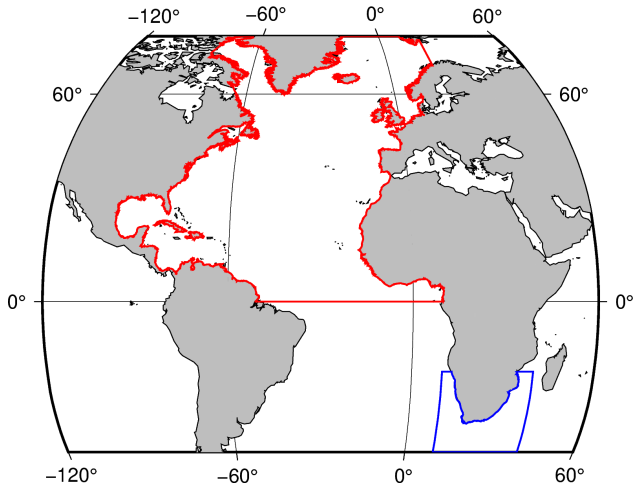

Figure 3.1: The two main study areas North Atlantic (red, region A) and Agulhas Current south of Africa (blue, region B)

66°N only CryoSat–2 observations with poor temporal resolution are available, consequently low quality estimates of the MSS is expected in this area.

Region B with the Agulhas Current is selected because of its high temporal variability and the smaller extent which allows to test the estimation of models on finer meshes limiting usage of computing time resources. The number of used observations inside the two study areas per mission is shown in the two last columns of Table 3.1. In total there are more than 58×10^6 observations inside region A and almost 5.5×10^6 inside region B. These observations are almost equally distributed over the time period and within the months of a year. Thus, it can be avoided that a year or a month is overrepresented in the data.

The two regions are shown in Figure 3.1. These boundaries are used to compute the triangulations (see Section 2.1.2). Figure 3.2 shows the meshes generated for each of the two study areas. Both meshes are computed with *jigsaw-geo* with a constant target edge length of 100 km at the equator, which corresponds to a edge length of about 1°.

3.2 Results

With the proposed approach presented above, it becomes possible to estimate either a static MSS model (cf. Eq. (2.1.1)) or a MSS model which co-estimates the temporal model component (cf. Eq. (2.3.4)). This study puts the focus on the time variable computation, with special focus on the specific model cf. Eq. (2.3.5). The reference epoch t_0 is chosen as January 1st, 2010. The numerical results obtained in this study are compared to the static CNES_CLS15 MSS (Pujol et al., 2018) product (cf. Eq. (2.3.8)) and the temporal model component (cf. Eq. (2.3.9)) to the delayed-time DUACS Level 4 gridded SLA DT2010 maps (cf. Dibarboure et al., 2012).

	start	end	ground track spacing	repeat cycle	#obs region A	#obs region B
CryoSat–2	01/2011	12/2019	~8 km	369 days	20.46 M	1.87 M
Jason–1	01/2010	03/2012	315 km	10 days	5.54 M	0.52 M
Jason–1 GM	05/2012	06/2013	7.5 km	406 days	2.78 M	0.27 M
Jason–2	01/2010	05/2017	315 km	10 days	18.95 M	1.79 M
Jason–2 GM	07/2017	09/2017	8.5 km	371 days	0.48 M	0.04 M
Jason–3	02/2016	12/2019	315 km	10 days	10.09 M	0.95 M

Table 3.1: Overview of some characteristics of the selected missions.

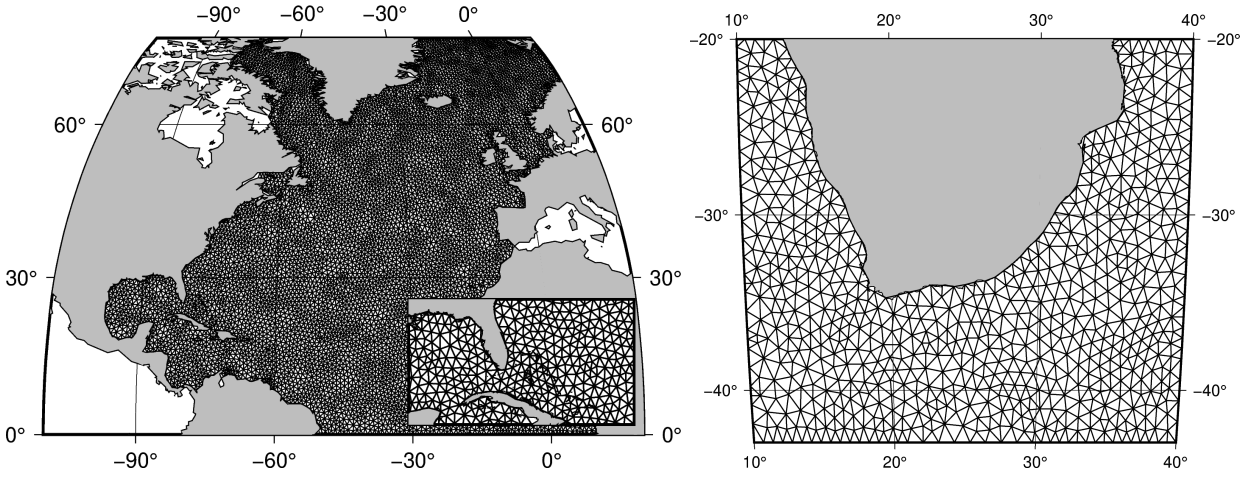

(a) (b)

Figure 3.2: Two meshes with a target edge length of 100 km at the equator inside the study area North Atlantic and inside the Atlantic Ocean and Indian Ocean south of Africa, generated with jigsaw-geo.

Scenario	Area	Finite Element	Mesh	Time Variability
B_{30}^{Arg}	South Africa	Argyris	30 km	$T = 365.25$ d
B_{40}^{Arg}	South Africa	Argyris	40 km	$T = 365.25$ d
B_{50}^{Arg}	South Africa	Argyris	50 km	$T = 365.25$ d
B_{100}^{Arg}	South Africa	Argyris	100 km	$T = 365.25$ d
B_{30}^{HCT}	South Africa	HCT	30 km	$T = 365.25$ d
B_{100}^{HCT}	South Africa	HCT	100 km	$T = 365.25$ d
$A_{100}^{\mathrm{Arg,static}}$	North Atlantic	Argyris	100 km	static
A_{100}^{Arg}	North Atlantic	Argyris	100 km	$T = 365.25$ d

Table 3.2: Description of the eight analyzed estimation scenarios.

To demonstrate the flexibility of the proposed approach, eight different estimations scenarios with different spatial and temporal characteristics are studied (cf. Table 3.2). Whereas the first six scenarios are applied to the smaller study region B with different spatial resolutions (30 km to 100 km meshes) and the HCT as well as the Argyris element, scenarios 7 and 8 cover the entire North Atlantic ocean with a quite coarse spatial resolution using a 100 km mesh ($A_{100}^{\mathrm{Arg,static}}$ and A_{100}^{Arg}).

To evaluate the usability and to demonstrate the advantages of the proposed method, the estimates for the scenarios, cf. Tab. 3.2, comparisons of the estimates to the global CNES_CLS15 MSS model and comparison of the time-variable component to gridded SLA products will be presented.

3.2.1 Validity Check of the Static Model Component

To study the results and the influences of the different scenario configurations, differences of the static i.e. mean part (cf. Eq. (2.3.8)) with respect to a global long-term MSS model are analyzed. To remove the major signal and to emphasize the details, the estimated models are evaluated on the grid provided with the CNES_CLS15 MSS model and the difference to CNES_CLS15 model is computed without accounting for the different reference epochs. Thus, in regions of large ocean variability and sea level change, larger differences are expected.

Figure 3.3 shows the estimated C^1-smooth MSS and the difference of the static part to CNES_CLS15 MSS of the scenario A_{100}^{Arg}. At first glance, the static part of the time variable model A_{100}^{Arg} visually

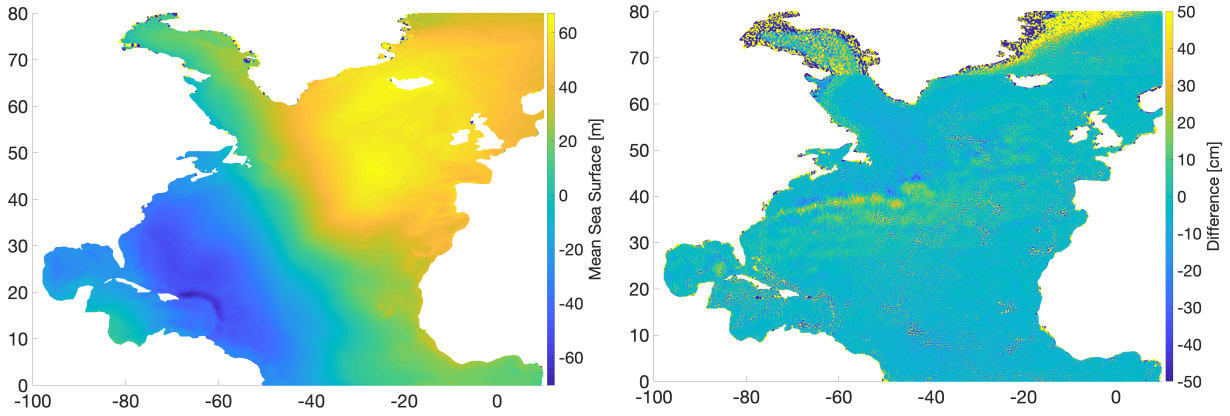

(a) (b)

Figure 3.3: Static part of the time variable estimation scenario A_{100}^{Arg} (a) and difference of this scenario to the reference model CNES_CLS15 MSS (b).

Scenario	Median	RMS	RMS R_1	RMS R_2	RMS R_3	RMS R_4	parameter
B_{30}^{Arg}	−1.9 cm	12.9 cm	3.8 cm	10.1 cm	16.0 cm	15.4 cm	68 996
B_{40}^{Arg}	−1.9 cm	11.3 cm	3.2 cm	8.4 cm	13.4 cm	14.1 cm	38 831
B_{50}^{Arg}	−1.8 cm	10.2 cm	2.9 cm	7.6 cm	11.7 cm	12.9 cm	25 138
B_{100}^{Arg}	−1.8 cm	8.9 cm	2.5 cm	7.0 cm	10.5 cm	11.3 cm	6575
B_{30}^{HCT}	−1.9 cm	11.2 cm	3.2 cm	8.5 cm	13.4 cm	13.8 cm	45 821
B_{100}^{HCT}	−1.7 cm	10.9 cm	3.8 cm	8.6 cm	14.4 cm	12.0 cm	4328

Table 3.3: Display of median and RMS of the differences to CNES_CLS15 MSS for different models and regions R_1 to R_4 and their number of parameter.

follows the marine geoid (cf. Fig. 3.3(a)). But, to emphasize small variations and inconsistencies the difference to the CNES_CLS15 MSS is shown in Fig. 3.3(b). Two different types of differences can be observed: i) differences due to the incomplete temporal modeling and the different reference epoch and b) differences due to an insufficient spatial resolution. The lack of temporal modeling is mainly visible in the Gulf Stream area where the differences are up to a few decimeters. A harmonic analysis of the daily SLA maps (see also Sect. 3.2.2) has shown that in the areas of high temporal variability, the modeled annual period is not necessarily the most dominant. In contrast to that in the regions of the Mid-Atlantic Ridge differences can be seen where the spatial resolution of the spatial finite element space is insufficient. This leads to a spatial smoothing effect, which results in high-frequency oscillations in the differences. Another effect can be seen above 66°N latitude, where no ERM data entered the estimation. Static and temporal model components cannot be separated in the estimation, which yields high uncertainties and unstable estimates, which show up as large differences. The RMS of the differences is 11.4 cm over the entire area, which shows a reasonable agreement in the context of a proof of concept of the presented method[2]. To demonstrate the flexibility of the proposed approach, a more detailed analysis of specific characteristics is shown for study region B.

Figure 3.4 focuses on study area B and the comparison of different spatial resolutions, which are realized by either choosing different meshes or different finite element basis functions. The displayed differences correspond to the finest meshes from scenarios B_{30}^{Arg} (Fig. 3.4(a)) and B_{30}^{HCT} (Fig. 3.4(c)) and the coarsest meshes from scenarios B_{100}^{Arg} and B_{100}^{HCT} (Fig. 3.4(b) and Fig. 3.4(d)). Thus, both upper models are estimated with Argyris elements and the lower using the HCT elements.

It is visible that all estimates follow the CNES_CLS15 MSS in a range of ±50 cm but most

[2]Note again that the reference epochs differ, it is approximately the end 2003, begin 2004 for CNES_CLS15 MSS.

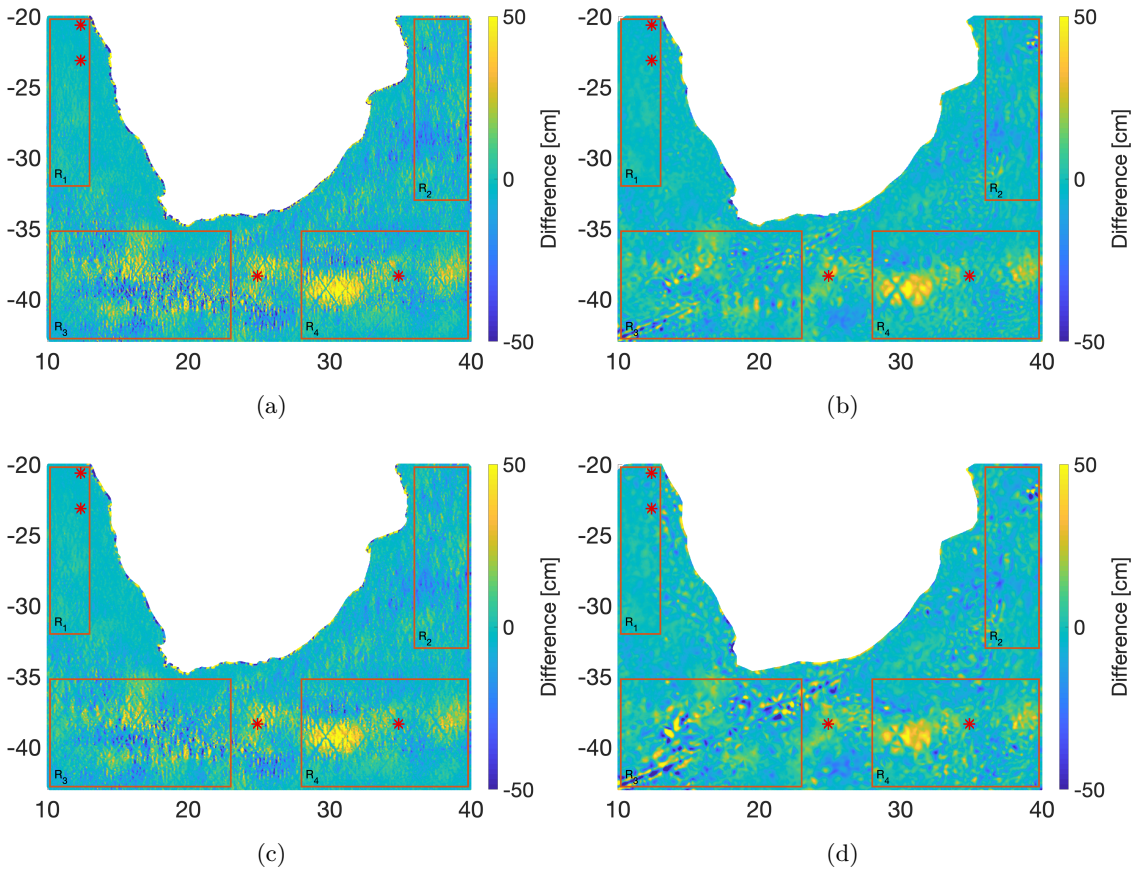

Figure 3.4: Differences between CNES_CLS15 MSS and the static part of four time variable models. The models correspond to the estimation scenarios B_{30}^{Arg} and B_{30}^{HCT} ((a) 30 km Argyris mesh and (c) HCT mesh) and B_{100}^{Arg} and B_{100}^{HCT} ((b) 100 km Argyris mesh and (d) HCT mesh). In addition, four further sub-regions R_1 to R_4 (orange) and four individual points (red stars) are shown.

parts outside the Agulhas current are in the range of just a few centimeters. The statistics from Tab. 3.3 confirm this with a root mean square error (after the reduction of the median which is about −1.9 cm) of 8.9 cm to 12.9 cm depending on the spatial resolution. A conspicuity between the differences is that the models on the coarser mesh are smoother than the models on the finer mesh. This is due to the different number of parameters of these models, especially for the temporal model component. The Argyris model on the coarse mesh with 6575 parameters uses less than a tenth parameters compared to the Argyris model on the finer mesh with 68 997. Although the static model requires the high spatial resolution to model the high-frequency – mainly geoid – signal, the spatial resolution seems too high for a stable estimation of the temporal component, which is limited by spatial sampling of the ERM. This leads to a more difficult separation of the temporal and spatial signal. As a result, the RMS is lowest for the 100 km meshes (8.9 cm and 10.9 cm) for Argyris and HCT, compared to the 30 km meshes (12.9 cm and 11.2 cm), see Tab. 3.3.

The same general features are visible in all four difference plots: a larger consistency in the northern area where less ocean variability is expected, and larger differences in the southern area within the Agulhas current where large ocean variability is expected. Consequently, the detailed differences are discussed separately for four different rectangular sub-regions R_1 to R_4, cf. Fig. 3.4. Tab. 3.3 lists the RMS values for the different regions as well.

For all models, largest consistency to the CNES_CLS15 MSS is visible in region R_1. The lowest RMS of 2.5 cm is as for the entire region B observed for the B_{100}^{Arg} model, which seems a reasonable quality measure for the approach presented here. As for the global view, the RMS slightly increases for the higher resolution scenarios which use the Argyris elements. In contrast to that, Fig. 3.4(d) shows the differences with respect to the B_{100}^{HCT} model, where additional differences – especially in the eastern part of R_1 – show up. Compared to the Argyris based models and the B_{30}^{HCT} scenario, an increase of the RMS is visible. From this, it can be concluded that the spatial resolution is insufficient to model the static signal. The degrees of freedom and the resulting flexibility of the Argyris element seem better suited to model the static MSS signal.

Within region R_2, more ocean variability is expected (e.g. cf. Fig. 3.8). Consequently, the consistency decreases, but still B_{100}^{Arg} shows the best agreement with an RMS of 7.0 cm. But, as for scenario B_{100}^{HCT} in region R_1, systematic differences start to show up in the north-eastern part. This serves as an indicator, that for the static part, the spatial resolution of the 100 km mesh is insufficient, as these differences vanish in the B_{30}^{Arg} scenario. But, as the model is in general less smooth, the overall RMS of B_{30}^{Arg} is higher (10.1 cm in R_2).

In region R_3, in addition to again higher ocean variability, higher resolution geoid signal is expected. As for R_2, although systematic differences now in the south-western part show up for B_{100}^{Arg} which are gone in B_{30}^{Arg}, the RMS of scenario B_{100}^{Arg} is still lowest. This differences are again attributed to static high-resolution (geoid) signal, which can not be captured with the Argyris element on the coarse mesh. When changing to the finer mesh – as in the B_{30}^{Arg} scenario – larger scale differences show up. These are attributed to a spatial over-parameterization of the time-variable model component, which is modeled with the same higher spatial resolution (30 km mesh).

Within region R_4, largest ocean variability is expected. Whereas all conclusions from R_1, R_2 and R_3 remain valid, the differences of all scenarios are dominated by a large scale large positive difference (yellow blob in Fig. 3.4) which dominates the RMS, such that it is the highest of all four sub-regions (11.3 cm for B_{100}^{Arg}). Within the large difference blob, the tracks of the ERM become clearly visible in form of a reduced difference along the ground track. Thus, consistency along the ERM repeat tracks is much higher. From this, it can be concluded, that the large difference is caused by high-frequency temporal variability in the GM data, which leaks into the static part as it is not fully captured by the trend and seasonal model applied in the scenarios.

With the proposed approach, reasonable estimates for the static component can be derived, although it is challenging to obtain the optimal spatial resolution, especially for the temporal model component, because of the insufficient temporal observation distribution outside of the ERM tracks. It is shown, that the temporal model (trend and seasonal component) is – at least in some sub-regions – insufficient to completely remove the ocean variability from the SSH observation of the non ERM. A striking advantage of this new method is the possibility to describe the continuous

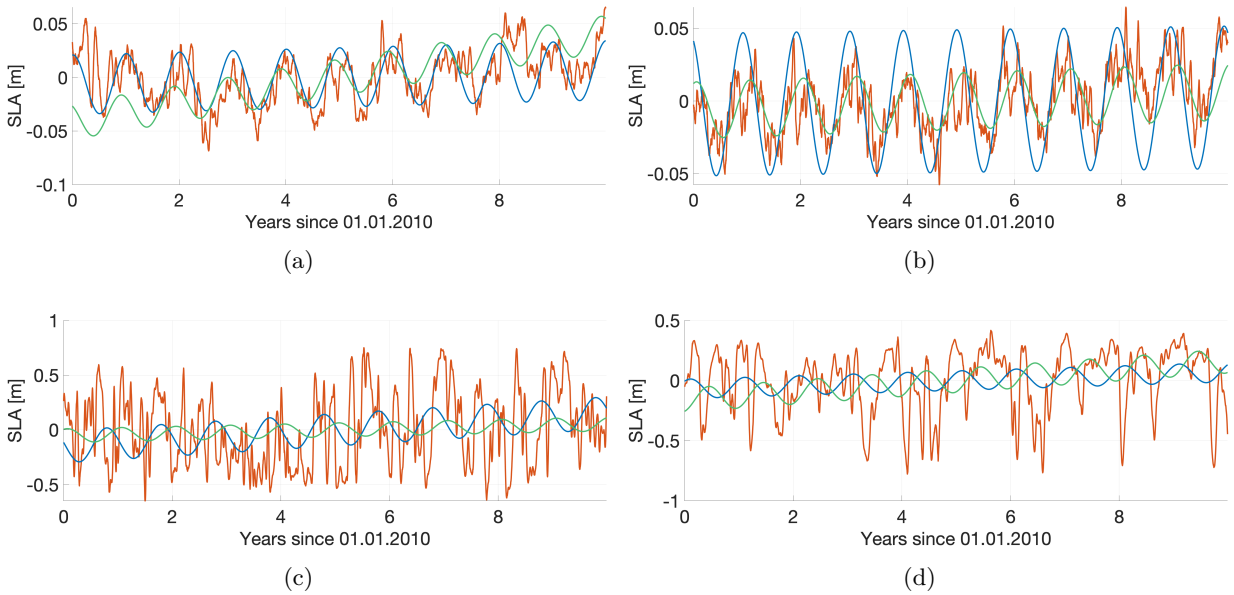

Figure 3.5: SLA time series (red) for four different locations with estimated time series at the same locations of the scenarios B_{30}^{Arg} (blue) and B_{100}^{Arg} (green).

surface (plus selected temporal characteristics) with just 4000 to 70 000 parameters. In contrast to this, the CNES_CLS15 MSS model is represented by about 1.7×10^6 grid points in the same area and 18.8×10^6 grid points in area A to describe the surface on an oversampled discrete grid.

3.2.2 Validity Check of the Temporal Model Component

The previous section has shown, that still some non-modeled temporal signals seem to enter the static part of the estimated models. This can especially be seen in areas with a high temporal variability such as in the area of the Agulhas current (cf. Fig. 3.8, R_3 and R_4). To visualize the estimated temporal signal Eq. (2.3.9) can be used to evaluate the model for a single location as a time series. This time series represents SLA, which can be compared to time series extracted from the mean reduced DUACS SLA maps. The product provides expected ocean variability with a high temporal resolution of 1 d. For this purpose, the temporal component of estimation scenario B_{30}^{Arg} and B_{100}^{Arg} is evaluated at different grid points (cf. Fig. 3.4) and compared to the time series in the same location as extracted from the DUACS SLA maps in Fig. 3.5.

The SLA (red) and estimated time series of the scenarios B_{30}^{Arg} (blue) and B_{100}^{Arg} (green) are shown for four different locations with different properties (cf. Fig. 3.4). The locations shown in Figures 3.5(a) and 3.5(b) are both located in the smooth region R_1 of lower temporal variability. It is visible that the time series is dominated by the annual period, which is represented by the estimated models very well. Whereas the amplitudes are generally smaller for the coarser B_{100}^{Arg} model. It seems that the amplitude is biased towards some strong high-frequency signals. The time series shown in 3.5(c) and 3.5(d) are located in regions R_4 and between regions R_3 and R_4 (cf. Fig. 3.8). It can be seen – and supported by a spectral analysis of the SLA – that the annual period is not necessarily the dominating one. Consequently, the trend and seasonal model applied does not fit the SLA time-series very well and only a minor part of the variations are captured. High-frequency variations leak into the static model (see again R_3 and R_4 in Fig. 3.4(a) and 3.4(b)) and the linear trend.

To obtain better results, future modelings require an extended model of the temporal variability. Increased temporal flexibility – more than the trend and the annual period – is required, which can be easily realized from a theoretical point of view by extending the set of temporal basis functions cf. (2.2.2). This entails an increased size of the parameter space, which can pose a computational problem.

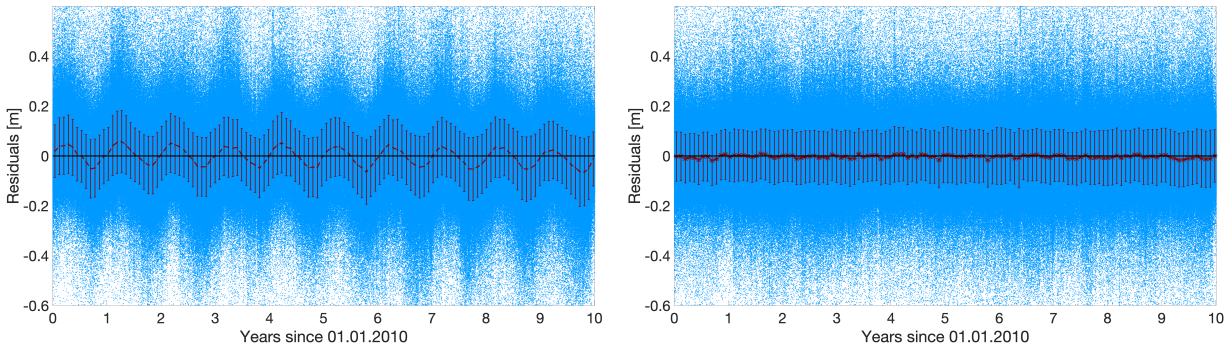

(a) Residuals of the static model

(b) Residuals of the time-variable model

Figure 3.6: Temporal representation of the least-squares residuals (blue) of scenarios $A_{100}^{\text{Arg,static}}$ and A_{100}^{Arg} with a 30 d moving average (red) and 1σ error bars derived from the standard deviation of each 30 d interval .

3.2.3 Validation on the Level of Least Squares Residuals

An additional measure of the model quality independent of a-priori models and other prior information are the least-squares residuals. They show how well the observations are described by the model. Figure 3.6 shows the least-squares residuals for the two scenarios computed for the North Atlantic, i.e. $A_{100}^{\text{Arg,static}}$ which just estimates the static MSS without the temporal model component and A_{100}^{Arg}, which co-estimates the linear trend and a seasonal component on the same 100 km mesh.

The first model ($A_{100}^{\text{Arg,static}}$) simply ignores the temporal variability and estimates the MSS in the North Atlantic with Argyris elements on a coarse 100 km mesh. The residuals are shown as a time series in Figure 3.6(a). An annual period in the observations (blue) and in the low-pass filtered mean (red) with an amplitude of approximately 5 cm is clearly visible and dominates the time-series. The second model (A_{100}^{Arg}) is estimated with the same mesh and same finite elements but models the trend and annual time variable parameters, cf. Eq. (2.3.5). Fig. 3.6(b) shows, pronounced by the low-pass filtered mean time series, that these additional parameters successfully modeled the annual signal and thus reduce the empirically estimated standard deviation. Although the additional parameters reduce the standard deviation only by 1 cm, i.e. from 11.5 cm to 10.5 cm, the residuals are less systematic.

To get an impression of the spatial characteristics of the least squares residuals, Fig. 3.7 shows the RMS of the residuals computed for $0.1°\times0.1°$ grid cells for both models as a measure of variability. At first glance, the plots for both models look very similar, i.e. the dominating features are visible in Figures 3.7(a) and 3.7(b). Four different aspects can be observed in the plots, which are generally valid for both models:

1. In most areas, the empirically estimated standard deviation of the residuals is in the order of 10 cm, which is a reasonable estimate for the standard deviation of a single SSH observation.

2. In the region north of 66° where only Cryosat-2 SSH observations are used, systematically larger standard deviations are visible. As a consequence of missing ERM data, the estimated model is of poor quality in those regions which results in large residuals.

3. There are regions of larger standard deviation which obviously correlate to high-resolution geoid signal, e.g. in the mid-Atlantic Ridge. This shows, that for some areas, the spatial resolution achieved with the Argyris elements on the 100 km mesh is insufficient to model all signal which is captured by the observations. At least locally, a higher spatial resolution is required.

4. Finally, there are regions with are affected by larger ocean variability (e.g. in the Gulf Stream along the U.S. East Coast or near the equator). Larger RMS are observed, as non-modeled temporal signal is absorbed the least-squares residuals.

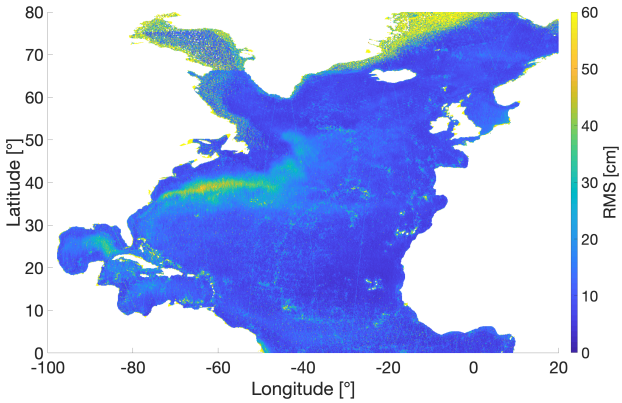

(a) RMS of the static model residuals per 0.1° grid cell.

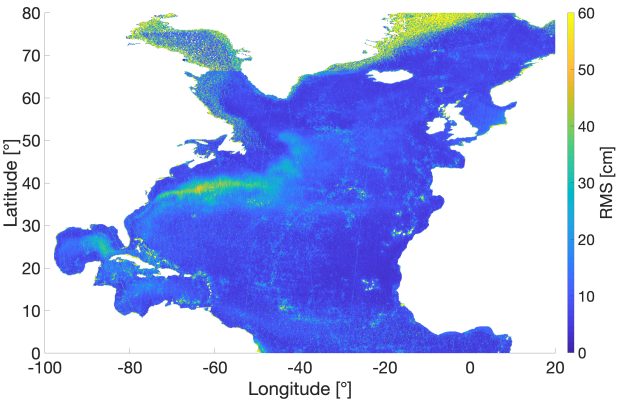

(b) RMS of the time-variable model residuals per 0.1° grid cell.

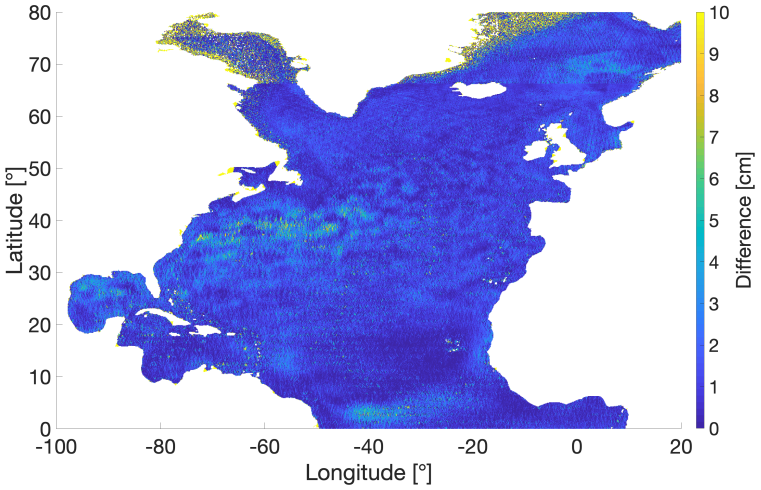

(c) Difference between the RMS of the static model residuals and the RMS of the time-variable model residuals per 0.1° grid cell.

Figure 3.7: Spatial representation of the RMS per 0.1° grid cell for a static and time-variable model.

To compare both models, Fig. 3.7(c) shows the difference of the gridded RMS values. A positive difference means that the spread of the residuals from the $A_{100}^{\text{Arg,static}}$ is larger compared to those of scenario A_{100}^{Arg}. As more than 85 % of the grid cells show a positive value, it can be concluded that the temporal model A_{100}^{Arg} successfully models temporal signal[3]. The reduction of the RMS is not uniquely distributed over the entire area, it is clearly concentrated in the regions with high temporal variability, e.g. the Gulf Stream, where the RMS is reduced by up to 10 cm and clearly shows the positive effect of co-estimating the temporal components in the model.

3.3 Additional Advantages of the Proposed Approach

3.3.1 Analysis of the Parameters

A special characteristic of the presented method is that due to the chosen parameterization of the finite elements, the parameters are interpretable. As the parameters in the static case correspond to function values, first derivatives etc. in the vertices of the mesh, this holds true for the temporal parameters as well.

Use of Equation (2.3.11) enables the display of the spatially varying parameters of the temporal basis functions (i.e. trend, amplitude and phase) as shown in Figure 3.8. For both the scenarios B_{30}^{Arg} and B_{100}^{Arg}, each of the aforementioned parameters was evaluated on a regular grid. Especially the parameters of the fine model (left column of Fig. 3.8) show a high spatial noise which is an additional indication of a spatial over-parameterization of the temporal signal, consequently data inconsistencies and noise are absorbed by the temporal component of the model. The parameters shown in the plots of the second column of 3.8 are smoother and show smooth spatial structures. One possibility to evaluate these results is to estimate trend, amplitude and phase of an annual period from the DUACS Level 4 gridded SLA DT2010 maps per grid cell. Plots of these are shown as reference in the right column of Fig. 3.8.

A visual comparison shows a correlation of the parameters – especially for the coarse model – to the reference plots, as similar structures are visible, especially for the seasonal signal. Whereas the trend estimates show similar spatial features, they are larger by an order of magnitude compared to the trends derived from the daily SLA product. Consequently, the trend parameters seem to significantly absorb higher frequency signal (see e.g. Fig. 3.5(c) where the trend seems to be affected by larger high-frequency amplitudes within the second half of the time series). In contrast to that, the magnitudes of the amplitudes are comparable and show a very similar spatial pattern. The phase displacement of both models show the same structures as that derived from the SLA grid.

A closer look to Fig. 3.8 shows additional problems along the coast and the artificial border of the region of interest (boundary of the mesh). This is on the one hand related to the lower quality of the SSH data close to the coast, but to a greater extent due to boundary effects, as the parameters along the border of the mesh are unconstrained. Consequently, observation sampling in the outer triangles of the mesh is poor and stable estimation of the parameters of the boundary nodes is not possible. This conclusion is supported by variance propagation (cf. Fig. 3.9), where the values along the boundary of the mesh show the highest formal standard deviations.

3.3.2 Description of the Model Uncertainty by Variance Propagation

Another advantage of the presented method – as it is a rigorous one-step least-squares procedure – is that it is straightforward to include a stochastic model of the SSH observations. With a realistic stochastic model, an accuracy estimate of the estimated MSS model in terms of a covariance matrix of the estimated parameters is possible. Applying variance propagation, this can be easily propagated to for instance the static MSS (cf. Eq. (2.3.8)).

Although in this proof-of-concept study the simplified assumption of uncorrelated SSH observations of same accuracy is used as stochastic model, variance propagation is applied as a plausibility

[3]Most cells, which show a negative value are located in the region above 66°, where the temporal model can not be stably estimated, as only Cryosat observations are available.

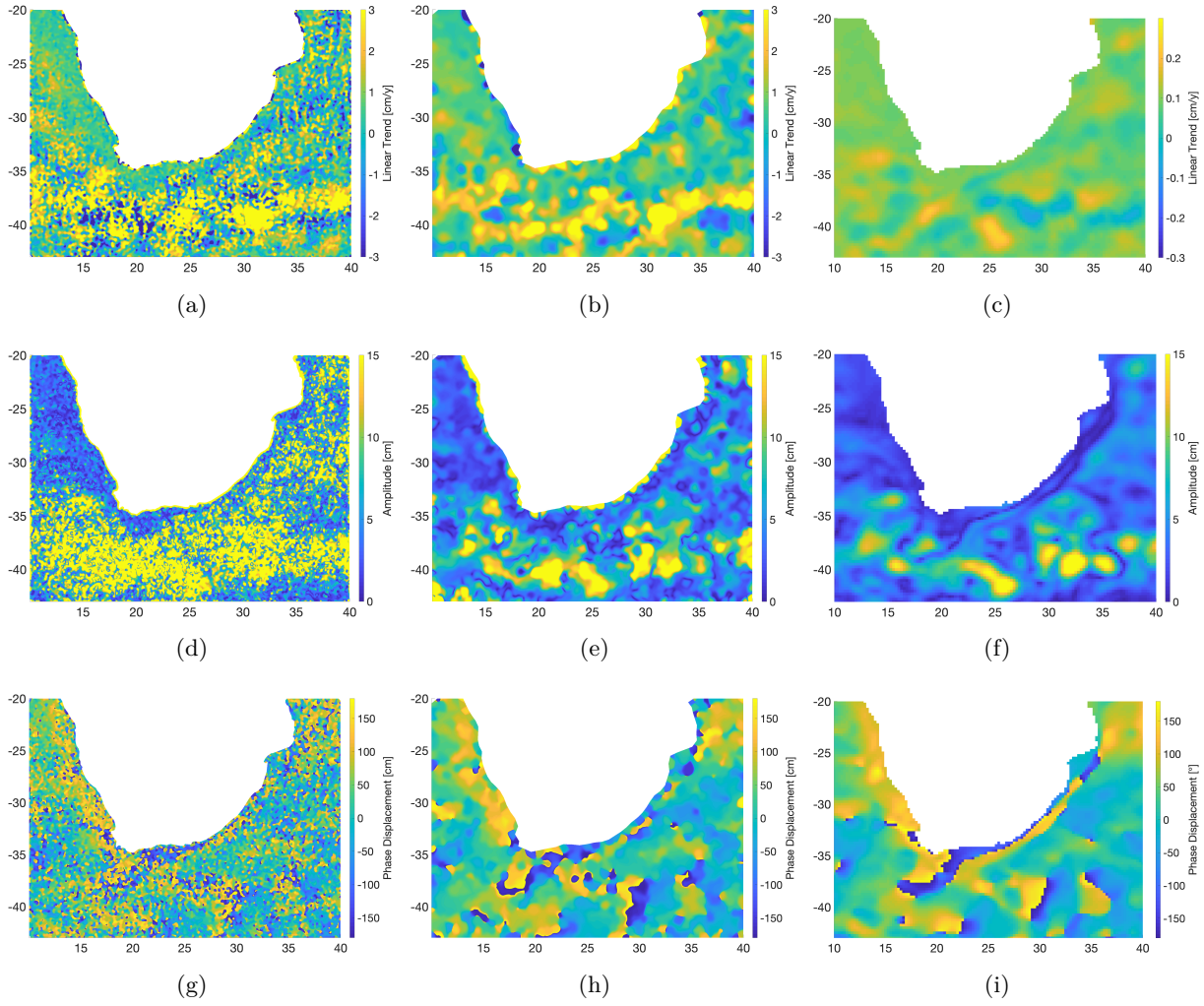

Figure 3.8: Spatial representation of the physical properties trend, amplitude and phase displacement of the two different models B_{30}^{Arg} (left column) and B_{100}^{Arg} (middle column). As comparison, trend, amplitude and phase maps as derived from the daily DUACS SLA maps are shown in the right column.

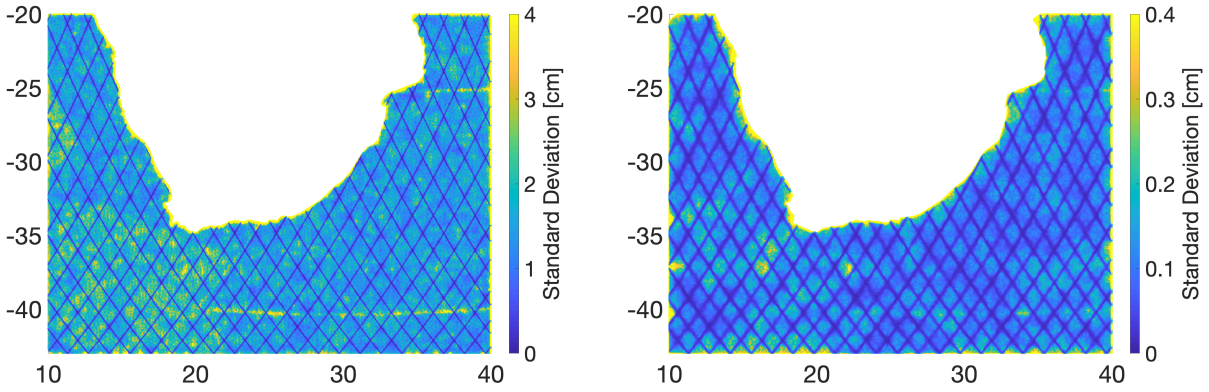

(a) (b)

Figure 3.9: Standard deviations of f_{mss} (c.f. Eq. (2.3.8)) of scenario B_{30}^{Arg} (a) and B_{100}^{Arg} (b) derived from variance propagation.

check here. The least squares estimate of the variance of unit weight is used to scale the covariance matrix of the parameters.

The standard deviations of f_{mss} (c.f. Eq. (2.3.8)) of scenarios B_{30}^{Arg} and B_{100}^{Arg} with an a priori accuracy of $\sigma_0 = 10\,\text{cm}$ for all observations are shown in Figure 3.9. This seems to be a reasonable guess because of the observation accuracy related to the models presented in section 3.2.3. Both models distinguish by a factor of 10 in their number of parameters to describe the model (cf. Fig. 3.3). The different number of parameters is visible in the coloration of both figures. Thus, the standard deviation of B_{30}^{Arg} (Fig. 3.9(a)) over the entire area is more than 10 times higher than the standard deviation of B_{100}^{Arg} (Fig. 3.9(b)) because the same number of observations are taken to estimate 10 times more parameters. Besides the ground tracks of the Jason missions are directly noticeable. Because of the short repeat cycle, resulting in higher number of observations in these areas, the standard deviations are comparatively smaller.

Chapter 4

Summary, Conclusions and Outlook

In this paper an approach for the estimation of a continuous spatio-temporal model of the mean sea surface from altimetric sea surface height observations is proposed. The continuous model is based on C^1-continuous finite element basis functions which represent the spatial signal. Finite elements defined on triangulations are used (Argyris and the HCT element) to assemble a continuous surface in the study region of interest. Substitution of the (unknown) scaling coefficients by one-dimensional parametric functions in the time domain constructs the proposed continuous spatio-temporal model. Within that model, the unknown scaling coefficients result from the Cartesian product of the temporal and spatial scaling coefficients of the basis functions, which are determined from the SSH observations within a least-squares parameter estimation process.

To demonstrate applicability and study the performance of the proposed approach, it is used to estimate a continuous model of the MSS. For this purpose 10 years of satellite altimetry data from CryoSat–2 (GM only) and Jason 1–3 (mainly ERM) collected in the period 2010 to 2019 is used. The approach estimates a static – i.e. mean – component as a C^1-continuous finite element model and co-estimates the temporal variability with the a linear trend and an annual signal with amplitude and phase. The temporal model component is used to absorb long-term temporal variability, especially from the sea surface height measurements from GM phases, consequently a reduction in advance is not required. Due to the parametric nature of the model, it can by synthesized on arbitrary grids and directly comes along with a tailored interpolator (in space and time). A re-parameterization of the finite elements is on the one hand usable to realize the C^1-smoothness for the composed function, but more important for the application to obtain physically interpretable parameters, which is the MSS and its derivatives for the static model component, and sea level trends, amplitudes and phases (and its derivatives) for the temporal model component. As the entire problem is formulated as a one step least-squares adjustment, stochastic characteristics of the observations can be easily included and propagated to uncertainties of the estimated model. However, due to a simplified stochastic model, this is just used as a plausibility check here.

This contribution can be seen as a proof-of-concept study for the application of the proposed procedure for MSS estimation. It is not (yet) the goal to estimate a best-quality MSS but to test the general performance and applicability of the approach. For this purpose, different meshes with different target edge length have been used in two study regions to estimate various MSS models which realize different spatial resolutions for the static as well as the temporal model component. The static model components have been compared to the CNES_CLS15 MSS and show an agreement within an RMS in the order of magnitude of 10 cm. The temporal model components were compared to gridded SLA products. Different systematic differences are visible, which are analyzed to identify indications for future model refinements required. It could be shown, that the seasonal component of the model successfully removes the annual signal from the observations. But, it has been shown, that the estimated annual period is not sufficient to describe the temporal variations of the ocean, especially in the areas of high oceanic variability where the annual period is not necessarily the dominant one, such as the Gulf and Agulhas Stream. The non-modeled signals, especially of large high-frequency variations leaked into the trend estimates, such that the trend tends to be over-estimated. But the estimated period was able to reduce the

overall RMS of the residuals by 1 cm in comparison to a static model which does not co-estimate temporal variations.

This work demonstrated that the approach is generally suited for MSS determination and identified the following points, which are necessarily refinements to derive high quality estimates MSS models which are competitive with models derived with the established state-of-the-art approaches:

- The temporal basis functions used here are very simple (trend and annual signal) and do not sufficiently remove the variability from the SSH measurements. Adding additional periods can allow for a better estimation of the temporal variability. But also the usage of a different temporal basis functions like B-Splines or one dimensional finite elements are worth to study and will add flexibility to model unexpected events like for instance the El Niño.

- It was shown that high spatial resolution is required to model the fine scale static signal. Currently, the spatial resolution of static and temporal component is the same. It could be identified, that a high spatial resolution (which successfully captures the fine-scale static signal) yields to a over-parameterization of the temporal component and thus to a poor overall performance. To obtain best possible quality, the approach needs to be refined to individually optimize the spatial resolution for the static (higher resolution) and the temporal component (lower resolution). This can be realized either with different meshes or smoothness constraints for the temporal model.

- Another possible improvement is to use data adaptive meshes especially in the static domain to reduce the parameter space and the risk of over-fitting. Thus, in regions with a smooth spatial signal, the mesh can be coarser than in regions with a high spacial variability.

- To obtain meaningful quality estimates of the estimated model, a data-adaptive stochastic model for the SSH observations is required. The least-squares residuals can be iteratively analyzed to estimated the stochastic information along the orbits for the individual altimetry missions and mission phases. This information can subsequently be used to build the covariance matrices.

Data availability statement The altimeter products were produced by Ssalto/Duacs and distributed by Aviso+, with support from CNES (`https://www.aviso.altimetry.fr`). The results from the proof of concept study will be made available on request, a persistent publication of the data set seems not reasonable at this stage.

Authors' contribution CN implemented the spatial finite element spaces and the basic framework used for the analysis. MB implemented the extension for temporal component of the model. CN, MB and JMB contributed to details of the implementation. CN, MB and JMB jointly designed the experiments. MB performed the data preparation, the computations and the analysis. MB prepared the draft of the manuscript. All authors contributed to interpretation and discussion of the results and improvement of the initial draft. JMB acted as scientific advisor.

Acknowledgements The authors acknowledge the financial support via the DFG project "*PArametric determination of the dynamic ocean topography from geoid, altimetric sea surface heights and SAR derived RAdial SURface Velocities*" (PARASURV, grant BR5470/1-1).

The authors gratefully acknowledge the Gauss Centre for Supercomputing e.V. (www.gauss-centre.eu) for funding this project by providing computing time through the John von Neumann Institute for Computing (NIC) on the GCS Supercomputer JUWELS at Jülich Supercomputing Centre (JSC).

The authors gratefully acknowledge the granted access to the Bonna cluster hosted by the University of Bonn.

Furthermore, the discussions with Till Schubert and Wolf-Dieter Schuh are gratefully acknowledged.

List of Figures

List of Tables

Bibliography

Agha Karimi A, Baltazar Andersen O, Deng X (2020) Mean Sea Surface and Mean Dynamic Topography Determination from Cryosat-2 Data around Australia. Advances in Space Research DOI 10.1016/j.asr.2020.01.009, URL http://www.sciencedirect.com/science/article/pii/S0273117720300272

Andersen O, Knudsen P, Stenseng L (2015) The DTU13 MSS (Mean Sea Surface) and MDT (Mean Dynamic Topography) from 20 Years of Satellite Altimetry. DOI 10.1007/1345_2015_182

Andersen O, Rose S, Knudsen P, Stenseng L (2018) The dtu18 mss mean sea surface improvement from sar altimetry. URL ftp://ftp.space.dtu.dk/pub/DTU18/MSS_MATERIAL/PRESENTATIONS/DTU18MSS-V2.pdf

Andersen O, Zhang S, Sandwell D, Gerald D, Smith W, Abulaitijiang A (2021) The unique role of the jason geodetic missions for high resolution gravity field and mean sea surface modelling. Remote Sensing 13:646, DOI 10.3390/rs13040646

Andersen OB, Knudsen P (2009) DNSC08 mean sea surface and mean dynamic topography models. Journal of Geophysical Research: Oceans 114(C11), DOI 10.1029/2008JC005179

Argyris JH, Fried I, Scharpf DW (1968) The tuba family of plate elements for the matrix displacement method. The Aeronautical Journal (1968) 72(692):701–709, DOI 10.1017/S000192400008489X

AVISO (2017) L2P SLA Product Handbook for missions Jason-3, OSTM/Jason-2, Jason-1, SARAL/AltiKa, Crysoat-2, HaiYang-2A, ERS-1, ERS-2, ENVISAT, Geosat Follow On, TOPEX/Poseidon. URL https://www.aviso.altimetry.fr/fileadmin/documents/data/tools/hdbk_L2P_all_missions_except_S3.pdf

Becker S, Freiwald G, Losch M, Schuh WD (2012) Rigorous fusion of gravity field, altimetry and stationary ocean models. Journal of Geodynamics 59–60:99–110, DOI 10.1016/j.jog.2011.07.006, URL http://www.sciencedirect.com/science/article/pii/S0264370711000834

Becker S, Losch M, Brockmann JM, Freiwald G, Schuh WD (2014) A Tailored Computation of the Mean Dynamic Topography for a Consistent Integration into Ocean Circulation Models. Surveys in Geophysics 35(6):1507–1525, DOI 10.1007/s10712-013-9272-9, URL http://link.springer.com/article/10.1007/s10712-013-9272-9

Chen JL, Shum CK, Wilson CR, Chambers DP, Tapley BD (2000) Seasonal sea level change from TOPEX/Poseidon observation and thermal contribution. Journal of Geodesy 73(12):638–647, DOI 10.1007/s001900050002, URL http://link.springer.com/article/10.1007/s001900050002

Ciarlet P (1978) The Finite Element Method for Elliptic Problems. Carnegie-Rochester Conference Series on Public Policy, North-Holland Publishing Company

Clough RW, Tocher JL (1966) Finite element stiffness matrices for analysis of plate bending pp p. 515–545

Dibarboure G, Schaeffer P, Escudier P, Pujol MI, Legeais JF, Faugère Y, Morrow R, Willis JK, Lambin J, Berthias P, Picot N (2012) Finding Desirable Orbit Options for the "Extension of Life" Phase of Jason-1. Marine Geodesy 35:363, DOI 10.1080/01490419.2012.717854, URL https://hal.archives-ouvertes.fr/hal-00798741

Dixon T, Naraghi M, Mcnutt M, Smith S (1983) Bathymetric prediction from seasat altimeter data. Journal of Geophysical Research Atmospheres 88, DOI 10.1029/JC088iC03p01563

Ducet N, Le Traon PY, Reverdin G (2000) Global high-resolution mapping of ocean circulation from topex/poseidon and ers-1 and -2. Journal of Geophysical Research: Oceans 105(C8):19477–19498, DOI 10.1029/2000JC900063, URL https://agupubs.onlinelibrary.wiley.com/doi/abs/10.1029/2000JC900063, https://agupubs.onlinelibrary.wiley.com/doi/pdf/10.1029/2000JC900063

Engwirda D (2014) Locally optimal Delaunay-refinement and optimisation-based mesh generation. PhD thesis, URL https://ses.library.usyd.edu.au/handle/2123/13148

Engwirda D (2017) Jigsaw-geo (1.0): Locally orthogonal staggered unstructured grid generation for general circulation modelling on the sphere. Geoscientific Model Development 10:2117–2140, DOI 10.5194/gmd-10-2117-2017

Engwirda D (2019) JIGSAW(GEO) is an unstructured mesh generator for geoscientific modelling.: Dengwirda/jigsaw-geo-matlab. URL https://github.com/dengwirda/jigsaw-geo-matlab

ESA (2020a) CryoSat-2 Product Handbook Baseline D 1.1. URL https://earth.esa.int/documents/10174/125272/CryoSat-Baseline-D-Product-Handbook

ESA (2020b) Jason-1. https://directory.eoportal.org/web/eoportal/satellite-missions/j/jason-1, last access: 2020-12-10

ESA (2020c) Jason-2. https://directory.eoportal.org/web/eoportal/satellite-missions/j/jason-2, last access: 2020-12-10

ESA (2020d) Jason-3. https://directory.eoportal.org/web/eoportal/satellite-missions/j/jason-3, last access: 2020-12-10

Jin T, Li J, Jiang WP (2016) The global mean sea surface model whu2013. Geodesy and Geodynamics 7, DOI 10.1016/j.geog.2016.04.006

Knudsen P, Bingham R, Andersen O, Rio MH (2011) A global mean dynamic topography and ocean circulation estimation using a preliminary goce gravity model. Journal of Geodesy 85:861–879, DOI 10.1007/s00190-011-0485-8

Le Traon PY, Dibarboure G (2004) An illustration of the contribution of the topex/poseidon—jason-1 tandem mission to mesoscale variability studies. Marine Geodesy 27:3–13, DOI 10.1080/01490410490489313

Mulet S, Rio MH, Etienne H, Artana C, Cancet M, Dibarboure G, Feng H, Husson R, Picot N, Provost C, Strub PT (2021) The new CNES-CLS18 Global Mean Dynamic Topography. Ocean Science Discussions pp 1–31, DOI 10.5194/os-2020-117, URL https://os.copernicus.org/preprints/os-2020-117/

Pujol MI, Schaeffer P, Faugère Y, Raynal M, Dibarboure G, Picot N (2018) Gauging the Improvement of Recent Mean Sea Surface Models: A New Approach for Identifying and Quantifying Their Errors. Journal of Geophysical Research: Oceans 123(8):5889–5911, DOI 10.1029/2017JC013503, URL https://agupubs.onlinelibrary.wiley.com/doi/abs/10.1029/2017JC013503

Schaeffer P, Faugére Y, Legeais JF, Ollivier A, Guinle T, Picot N (2012) The cnes_cls11 global mean sea surface computed from 16 years of satellite altimeter data. Marine Geodesy 35(sup1):3–19, DOI 10.1080/01490419.2012.718231, URL https://doi.org/10.1080/01490419.2012.718231, https://doi.org/10.1080/01490419.2012.718231

Smith W, Sandwell D (1994) Bathymetric prediction from dense altimetry and sparse shipboard bathymetry. Journal of Geophysical Research 992, DOI 10.1029/94JB00988

Traon PY, Nadal F, Ducet N (1998) An improved mapping method of multisatellite altimeter data. Journal of Atmospheric and Oceanic Technology - J ATMOS OCEAN TECHNOL 15:522–534, DOI 10.1175/1520-0426(1998)015<0522:AIMMOM>2.0.CO;2

Uebbing B, Kusche J, Rietbroek R, Landerer FW (2019) Processing Choices Affect Ocean Mass Estimates From GRACE. Journal of Geophysical Research: Oceans 124(2):1029–1044, DOI 10.1029/2018JC014341, URL https://agupubs.onlinelibrary.wiley.com/doi/abs/10.1029/2018JC014341